10 Precipitation

In the previous three chapters, we discussed how cloud droplets and ice crystals form on the microscale and how they can grow large enough to initiate precipitation. Precipitation denotes any kind of hydrometeors reaching Earth's surface, including drizzle, rain, snow, graupel, and hail. Drizzle, rain, snow, graupel, and hail are the generic terms: the entirety of drizzle drops is called drizzle, of raindrops rain, of snowflakes snow, of graupel particles graupel, and of hailstones hail. In the global mean, only 1 in 11 clouds forms precipitation. Thus, dissipating clouds are much more common than precipitating ones (Pruppacher and Jaenicke, 1995).

In this chapter, we take a more macroscopic perspective and start with common raindrop and snowflake size distributions (Section 10.1) followed by an overview of observed precipitation rates (Section 10.2), measured with rain gauges at Earth's surface.

We explain how estimates of precipitation rates can be obtained from radar measurements and how radar images can be interpreted (Section 10.3). Next, we classify precipitation into stratiform and convective precipitation (Section 10.4) and explain its mesoscale structure (Section 10.5). The chapter concludes with a discussion of the geographical distribution of precipitation in the present climate, how it has changed since the 1950s, and how it is projected to change until the end of this century (Section 10.6).

10.1 Number Size Distributions of Hydrometeors

10.1.1 Raindrop Number Size Distribution

Field observations of raindrop size distributions can, for instance, be made acoustically with the Joss–Waldvogel disdrometer (Joss and Waldvogel, 1967), which converts the kinetic energy of a raindrop impacting on a membrane into an electric pulse whose amplitude is a function of the raindrop size. The electric pulses are then converted into an estimated raindrop number size distribution. At Earth's surface, typical raindrop number size distributions (Figure 10.1) show a rapid decrease in drop number concentration with increasing size for the equivalent raindrop diameter D_{eq} larger than 1 mm, due to raindrop break-up and because generally fewer large drops are formed. Note that we use diameter in Section 10.1 for consistency with the relevant literature. Different raindrop size distributions have been observed: exponential (Marshall and Palmer, 1948), gamma (Ulbrich, 1983), and log-normal (Feingold and Levin, 1986). Exponential raindrop size distributions, which are good proxies for climatological values, can be described by the so-called Marshall–Palmer distribution (Marshall and Palmer, 1948):

$$n_N(D_{eq}) = N_0 \exp(-\Lambda D_{eq}), \tag{10.1}$$

https://doi.org/10.1017/9781009485654.011 Published online by Cambridge University Press

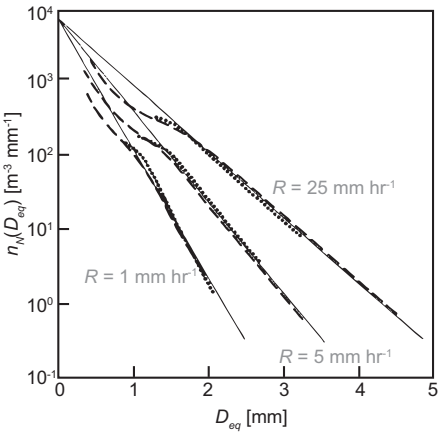


Figure 10.1 Measured raindrop number size distributions $n_N(D_{eq})$ (dashed and dotted lines) for different rainfall rates R_r as a function of the equivalent diameter of the raindrops D_{eq}, together with best-fit exponential curves (solid lines). Figure adapted from Marshall and Palmer (1948). Published (1948) by the American Meteorological Society.

where $n_N(D_{eq})$ is the number concentration of raindrops per unit length, N_0 is the intercept parameter in cm^{-4} and Λ is the slope of the raindrop size distribution in m^{-1} or cm^{-1}. We note that the Marshall–Palmer distribution given by eq. (10.1) is a special case of the gamma distribution (eq. 1.1) with $\mu = 0$.

To obtain the total number of raindrops, eq. (10.1) needs to be integrated over the equivalent diameter range dD_{eq}: $N = \int n_N(D_{eq}) dD_{eq}$. Marshall and Palmer (1948) found the following empirical dependence of Λ on the rainfall rate R_r:

$$\Lambda(R_r) = c_r R_r^{-0.21}, \tag{10.2}$$

where R_r is in mm h^{-1}, Λ is in cm^{-1}, and $c_r = 41\,\text{cm}^{-1}(\text{mm h}^{-1})^{0.21}$.

Marshall and Palmer (1948) observed a rather constant intercept parameter $N_0 = 0.08\,\text{cm}^{-4}$, which is independent of the precipitation rate, as shown in Figure 10.1. The dependence of Λ on the rainfall rate indicates that the raindrop size distribution changes with rainfall intensity in such a way that the higher R_r is, the smaller Λ becomes. This means that $n_N(D_{eq})$ decreases less quickly at higher rainfall rates (Figure 10.1). Higher rainfall intensities are caused by higher updraft speeds in clouds and hence higher liquid water contents, which produce larger raindrops. It has been found that the Marshall–Palmer distribution does not hold true for small raindrops (Waldvogel, 1974; Feingold and Levin, 1986; Willis and Tattelman, 1989). This is also noticeable in the data shown in Figure 10.1, which show deviations from the exponential distribution at equivalent diameters below 1.6 mm.

https://doi.org/10.1017/9781009485654.011 Published online by Cambridge University Press

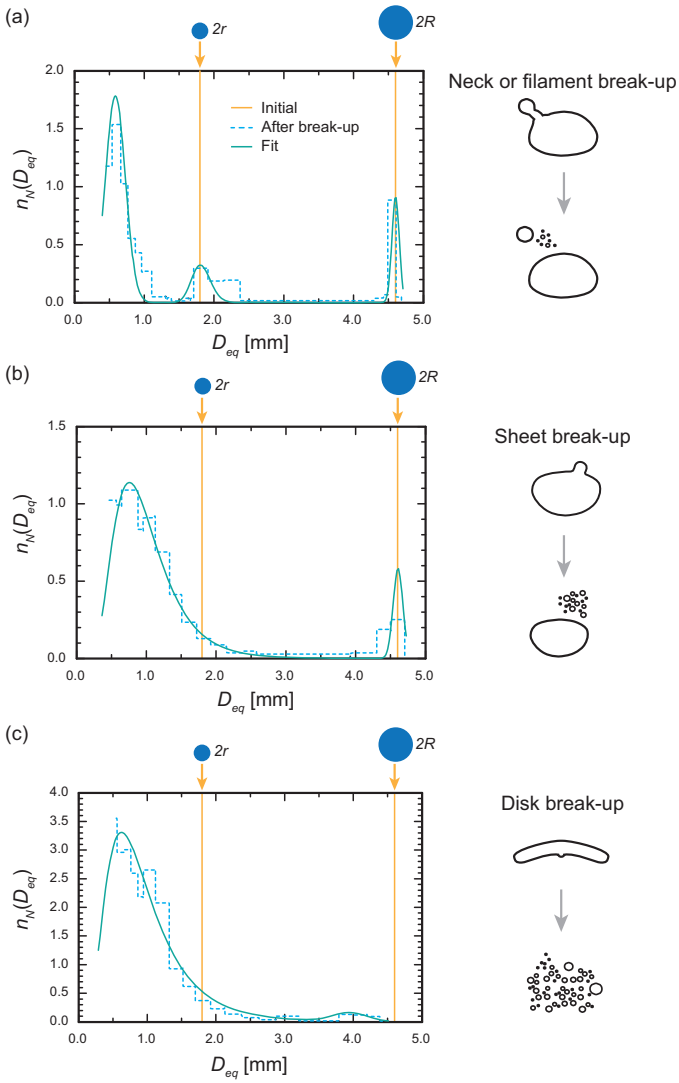


Figure 10.2 Examples from laboratory experiments of average number size distributions of raindrop fragments $n_N(D_{eq})$, in numbers per size interval (0.2 mm) as a function of raindrop equivalent diameter D_{eq}. The fragments were produced by (a) neck or filament break-up, (b) sheet break-up, and (c) disk break-up (Figure 8.18). The measurements are shown as dashed lines and distributions fitted to the data as solid lines. The original D_{eq}'s of the raindrops (1.8 mm and 4.6 mm) are indicated by the vertical lines. Note the different vertical scales. Figure adapted from Low and List (1982). ©American Meteorological Society. Used with permission.

Raindrops falling through a cloud hardly interact with other raindrops because their number density is much lower than that of cloud droplets. On average, there is only one raindrop in a million cloud droplets (Figure 8.1). Raindrops may experience some shrinking due to evaporation when the RH below cloud is less than 100 % or due to break-up (Section 8.3) upon collision with other hydrometeors. Figure 10.2 shows an example of averaged measured size distributions after raindrop break-up (Section 8.3.4), as obtained from laboratory experiments (Low and List, 1982). The collisions resulted from a raindrop of $D_{eq} = 4.6$ mm with a raindrop of $D_{eq} = 1.8$ mm. For neck or filament break-up, a third peak consisting of satellite drops (Figure 10.2a) appears at around $D_{eq} = 0.6$ mm in addition to the two peaks centered at the original raindrop sizes. Sheet break-up is effective in removing the smaller drop from the distribution whereas the larger drop keeps its identity (Figure 10.2b).

https://doi.org/10.1017/9781009485654.011 Published online by Cambridge University Press

Disk break-up has the highest CKE (eq. 8.66) and thus creates the largest number of small satellite drops by eliminating the identities of both colliding drops (Figure 10.2c).

10.1.2 Snowflake Number Size Distribution

Raindrops can originate from melted ice hydrometeors (snow, graupel, hail). In the absence of an ice phase, raindrop formation requires the collision–coalescence process due to the slow diffusional growth of water droplets. Unlike raindrops, individual ice crystals can grow large enough by diffusional growth to precipitate and reach Earth's surface. A phenomenon that is observed in otherwise clear or nearly clear skies is called "diamond dust" or "clear-sky ice precipitation" (Section 9.3.1). Diamond dust can occur anywhere in the world where the temperatures are well below 0 °C, but is most common in the polar regions (Intrieri and Shupe, 2004; Santachiara et al., 2016). For example, in the Arctic, it has been observed to occur approximately 13 % of the time during winter and not at all during summer (Intrieri and Shupe, 2004).

For single dendrites or irregular aggregates of crystals, there is no easy way to measure their linear dimension. Thus, data on snowflakes are usually expressed in terms of particle mass or equivalent diameter D_{eq} of the drop formed from the melted snowflake. An example of a snowflake number size distribution in terms of D_{eq} is shown in Figure 10.3. As in the case for rain (eq. 10.1), the snowflake size distribution has been found to be exponential (Gunn and Marshall, 1958):

$$n_N(D_{eq}) = N_0 \exp(-\Lambda D_{eq}). \tag{10.3}$$

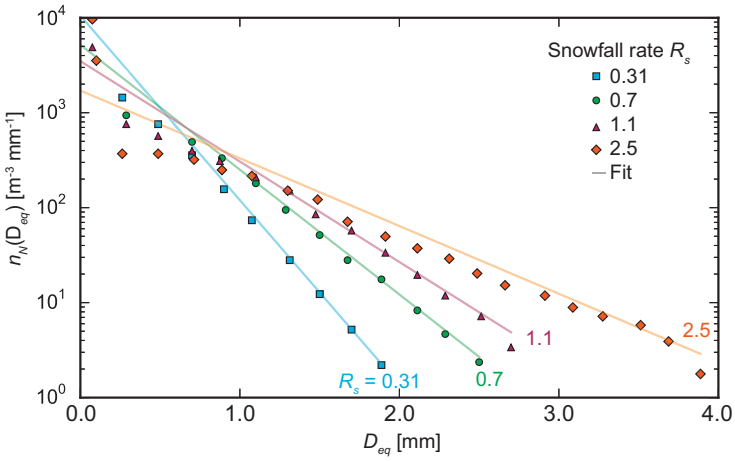


Figure 10.3 Number size distributions of snowflakes $n_N(r_{eq})$ expressed in terms of melted equivalent diameter D_{eq} as a function of the snowfall rate R_s in mm h^{-1}. Figure adapted from Gunn and Marshall (1958). Published (1958) by the American Meteorological Society. Used with permission.

https://doi.org/10.1017/9781009485654.011 Published online by Cambridge University Press

For snow, however, the intercept parameter N_0 in cm^{-4} is not constant but depends on the snowfall rate R_s in $\mathrm{mm\,h}^{-1}$, here expressed as the water-equivalent depth of the accumulated snow:

$$N_0 = c_N R_s^{-0.87}; \qquad \Lambda(R_s) = c_s R_s^{-0.48}, \tag{10.4}$$

with $c_N = 0.038\,\mathrm{cm}^{-4}\,(\mathrm{mm\,h}^{-1})^{0.87}$ and $c_s = 25.5\,\mathrm{cm}^{-1}\,(\mathrm{mm\,h}^{-1})^{0.48}$. The number size distribution of snow particles for a given precipitation rate was found to be broader than for raindrops (Gunn and Marshall, 1958). The reason for this is that snowflakes can grow considerably larger than raindrops, because they usually grow in environments that are highly supersaturated with respect to ice, such that their growth by diffusion is more efficient than that of raindrops. In addition, snowflakes have smaller fall velocities (Section 9.3.2), less CKE upon collision, and less readily break into pieces. Nevertheless, the fracturing of snowflakes can occur as one mechanism of ice multiplication (Section 9.4). While fracturing of raindrops is only a function of droplet size and the relative fall velocity of the colliding hydrometeors, the fracturing of snowflakes depends not only on crystal size, but also on crystal density and habit, as well as temperature (Korolev and Leisner, 2020), making snowflake number size distributions overall more variable.

10.2 Precipitation Rates

Regardless of if precipitation is initiated via warm or cold microphysical processes inside clouds, over a large part of Earth's surface it reaches the ground as rain because the average surface temperature of Earth is 16 °C (Forster et al., 2021).

The intensity of precipitation is expressed in terms of a precipitation rate R_p, which is the volume flux of precipitation through a horizontal surface per unit time interval. It has units of $\mathrm{m^3\,m^{-2}\,s^{-1}} = \mathrm{m\,s^{-1}}$, but is usually expressed either in $\mathrm{mm\,h^{-1}}$ or in $\mathrm{mm\,day^{-1}}$. The precipitation rate is given by:

$$R_p = \frac{4}{3}\pi \int_{r_h=0}^{r_h=\infty} n_N(r_h) r_h^3 v_T(r_h) dr_h, \tag{10.5}$$

where $n_N(r_h)$ is the number size distribution of hydrometeors and $v_T(r_h)$ is the terminal velocity of a hydrometeor with radius r_h. This equation can be applied to both rain and frozen precipitation (snow, graupel, and hail). For the latter, r_h refers to the equivalent radius of the melted snowflakes, and R_r denotes the equivalent rainfall rate, expressed in $\mathrm{mm\,h^{-1}}$ of melted water. Here, equivalent rainfall rate means that all the frozen precipitation is assumed to have been melted.

Values of R_r vary from trace amounts to up to several hundred $\mathrm{mm\,h^{-1}}$. Light precipitation (i.e., drizzle) typically has rainfall rates below $1\,\mathrm{mm\,h^{-1}}$ (e.g., Comstock et al., 2007). Rainfall rates in excess of about $10\,\mathrm{mm\,h^{-1}}$ are associated with convective showers[1] or storms (see also Table 10.3). At most locations, annual snowfall rates tend to be at least an order

[1] https://community.wmo.int/en/activity-areas/aviation/hazards/precipitation

https://doi.org/10.1017/9781009485654.011 Published online by Cambridge University Press

of magnitude lower than rainfall rates for two reasons: (i) terminal velocities of snowflakes are an order of magnitude lower than those of raindrops (Figure 9.18), decreasing snowfall rates in a given precipitation event as compared to rainfall rates and (ii) for snow to reach Earth's surface as solid precipitation, the wet-bulb temperature (Section 3.5.7) near Earth surface ground needs to be below 2 °C (Häggmark et al., 2000; Wang et al., 2019). The wet-bulb temperature matters here, because it indicates the temperature that can be reached due to evaporation/sublimation of hydrometeors. For a given temperature, more latent heat is consumed due to sublimation at lower RHs, and hence the snow has a higher chance to remain solid. In most locations, such low temperatures occur far less often than higher temperatures in the annual mean. Nevertheless, it can certainly still happen that snowfall rates exceed rainfall rates for a single precipitation event.

Globally, precipitation rates vary greatly: Arica in western Chile is the driest place on Earth with 0.76 mm observed annual precipitation[2]. It also holds the record for the longest dry period. No precipitation fell for 172 months, from October 1903 to January 1918[3]. Cherrapunji in eastern India holds the record for the most precipitation ever observed in one year, when 26 470 mm fell between August 1860 and July 1861[4] owing to monsoonal rainfall associated with orographic uplift.

10.3 Radar

Microwave radars were developed early in World War II to aid spotting distant ships and airplanes, but their usefulness in meteorology quickly became clear. Pioneers like John Stewart Marshall (Marshall et al., 1947) and David Atlas (Atlas, 1964) were among the first to quantitatively measure precipitation quantitatively using radars. Nowadays, precipitation radars are an essential measurement tool for weather services globally (Browning, 1983; Kidd and Huffman, 2011; Barton et al., 2020). While rain gauges measure precipitation rates only at individual measurement sites, radars can detect precipitation over large areas and can provide advanced warnings for hazardous weather (e.g., Thorndahl et al., 2017). In fact, radars are irreplaceable for short-term forecasts because they reveal information about the mesoscale structure of precipitation. This is called *nowcasting* of precipitation events (e.g., Turner et al., 2004; Bowler et al., 2006; Ayzel et al., 2020).

Radar stands for RAdio Detection And Ranging and uses active remote sensing. Remote sensing means that the instrument is in a location different from the objects (e.g., hydrometeors) to be detected. In active remote sensing instruments, radiation in the form of an electromagnetic pulse is sent toward the hydrometeors and their back-scattered signal is measured. In contrast, passive remote sensing refers to instruments that do not actively send out an electromagnetic pulse, but rather measure reflections of shortwave radiation or emission of longwave radiation from atmospheric gases, aerosol particles, or hydrometeors.

[2] https://wmo.asu.edu/content/south-america-lowest-average-annual-precipitation
[3] https://wmo.asu.edu/content/world-longest-recorded-dry-period
[4] https://wmo.asu.edu/content/world-meteorological-organization-global-weather-climate-extremes-archive

https://doi.org/10.1017/9781009485654.011 Published online by Cambridge University Press

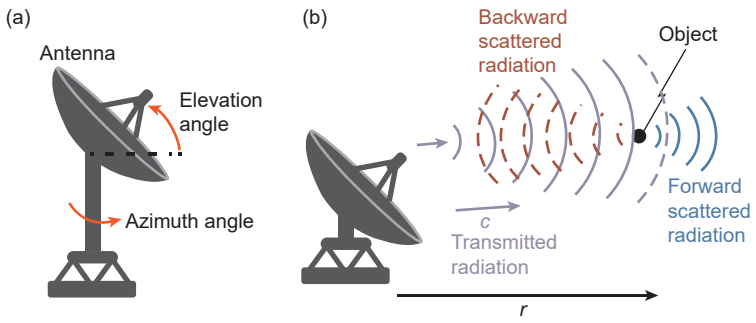


Figure 10.4 Schematic of a radar device showing (a) the rotation of the radar antenna around an azimuthal angle in the horizontal and an elevation angle in the vertical direction, and (b) the transmission of radiation with the velocity of light c, which is then scattered by an object at distance r away from the radar device.

The electromagnetic pulse sent out in radar measurements is intercepted by the (scattering) objects, as schematically shown in Figure 10.4. Part of the radiation is scattered forward and lost to the radar antenna. The radiation that is scattered backwards to the antenna is focused and recorded by a receiver. Information about the distance of the scattering objects from the radar instrument can be obtained from the time difference between sending out and receiving the electromagnetic pulse, which travels with the speed of light ($c = 3 \times 10^8\,\mathrm{m\,s^{-1}}$). This time difference is called the run time of the electromagnetic pulse. In addition, information on the radar reflectivity Z, the Doppler velocity v_D, and the linear depolarization ratio (LDR) can be obtained, as explained later.

In the Rayleigh regime (Section 2.1.3), the backscattered signal detected by the radar is proportional to the sixth power of the size r of the object (e.g., Kollias et al., 2007). Because of the large size dependence of Rayleigh scattering, cloud droplets and small ice crystals (in the size range of μm) cannot be detected with the same wavelength as precipitation particles (in the size range of mm, Table 1.2): if the radar echo (backscattered radiation) from precipitation particles is detected, the radar echo from cloud droplets is too weak due to the r^6 dependence. In fact, this strong dependence of the intensity of backscatter on the object size allows the specific detection of precipitation particles, because if it were only number-dependent, the abundant cloud droplets would far outweigh the signal compared to the few precipitation particles (Figure 8.1). To observed differently sized objects, radars with different wavelengths are used (Fabry, 2015; Battaglia et al., 2020). The most common are precipitation or weather radars (e.g., Barton et al., 2020), emitting electromagnetic pulses with wavelengths between 1 and 10 cm. Cloud radars with shorter wavelengths, in the millimeter range, are used to detect cloud droplets, ice crystals, and light drizzle (Kollias et al., 2007, 2016).

Both cloud and precipitation radars are not only used as ground-based systems, but have been employed on satellites in space, where they provide paramount information on the Earth's energy budget and hydrological cycle (Battaglia et al., 2020). The CloudSat Cloud Profiling Radar (Stephens et al., 2002), providing information on the spatial cloud coverage (Section 1.1.2), is one example of a spaceborne radar system. Some common radars together

https://doi.org/10.1017/9781009485654.011 Published online by Cambridge University Press

Table 10.1 Frequencies, wavelengths λ, and bands for various radars with typical applications.

Frequency	λ	Band	Radar	Application
94 GHz	3 mm	W-band	Cloud	Vertically pointing cloud radar (Stephens et al., 2002; Ramelli et al., 2024)
35 GHz	8.5 mm	Ka-band	Cloud or precip.	Scanning cloud/precipitation radar (Myagkov et al., 2016)
16–20 GHz	1–2 cm	Ku-band	Precipitation	Satellite-based Global Precipitation Measurement (GPM) program (Nakamura, 2021)
8–16 GHz	2–4 cm	X-band	Short-range (few tens of km) precip.	Weather services (Germann et al., 2022)
4–8 GHz	4–7 cm	C-band	Long-range precip.	Weather services (Germann et al., 2022)
2–4 GHz	7–15 cm	S-band	Long-range precip.	Weather services (Germann et al., 2022)

with their typical frequency and wavelengths are summarized in Table 10.1. Next to containing information on the size of the scattering objects, the radar signal can also contain information about the shape of the scattering objects. For example, dual-polarization radars transmit and receive horizontally and vertically polarized electromagnetic waves. Depending on the object, the electromagnetic wave either changes its orientation upon reflection or not. Having this additional information increases the quality of the radar data because it allows for a better classification of the different hydrometeor types: Detection of the shapes of the scattering objects allows to discriminate spherical water droplets from aspherical ice particles (Seifert et al., 2010; Besic et al., 2018; Kalesse-Los et al., 2022). It is also used to distinguish ground clutter, birds, and insects from hydrometeors.

For the purpose of illustrating the principle of radar measurements and its use to obtain precipitation rates or classify precipitation types, we constrain our discussion to ground-based weather radars in the following. However, the principal concepts apply to all radar systems.

10.3.1 Radar Reflectivity

The backscattered power of every individual hydrometeor within the radar volume depends on the properties of the hydrometeors. These are described by the backscattering cross section $\sigma_B(r_h)$, which depends predominantly on the hydrometeor size, r_h, but also on the hydrometeor projected area, density, phase, and shape. Assuming a perfectly spherical hydrometeor with $r_h \ll \lambda$ ($x \ll 1$) such that Rayleigh scattering (Section 2.1.3) can be assumed, $\sigma_B(r_h)$ is given by:

$$\sigma_B = \frac{64\pi^5 |K|^2 r_h^6}{\lambda^4}, \tag{10.6}$$

where λ is the radar wavelength. Here $|K|^2$ is the dielectric factor (Smith, 1984), which is the square of the absolute value of the complex index of refraction, describing how electromagnetic radiation propagates through the hydrometeor. It depends on the radar wavelength and the

https://doi.org/10.1017/9781009485654.011 Published online by Cambridge University Press

hydrometeor phase, that is, $|K|^2$ is different for water and ice: For liquid water $|K|^2 = 0.93$, which denotes the dielectric factor for water for the usual meteorological radar wavelengths (Smith, 1984). The actual dielectric constant of solid ice is $|K|^2 = 0.176$, if the particle sizes are expressed in equivalent ice sphere radii. However, assuming solid ice particles with a density identical to bulk ice is only a reasonable approximation for hail particles (Herman and Battan, 1961) because atmospheric ice crystals often have an effective density that is lower than that of bulk ice. Thus, the refractive index of ice crystals, and hence their dielectric factor, is usually better approximated by a homogeneous mixture of air and ice (Marshall and Gunn, 1952), a method that is often referred to as "soft sphere approach" (Liu, 2004). If solid hydrometeor sizes are expressed in terms of melted drop radii instead of equivalent ice sphere radii, then the dielectric constant of solid hydrometeors is $|K|^2 = 0.208$. Here, we stick to the latter and use $|K|^2 = 0.208$ for solid hydrometeors.

The power received at the radar antenna $\overline{P}_R$ averaged over a time interval of approximately 10 ms is given as

$$\overline{P}_R = C_R \frac{Z|K|^2}{D_{RT}^2}. \tag{10.7}$$

The power depends on the radar reflectivity factor Z given in units of $\mathrm{mm^6\,m^{-3}}$ and decreases quadratically with distance D_{RT} between the scattering object and the radar. C_R comprises constants and radar parameters: its wavelength λ, peak power, gain, pulse duration, and beamwidth (Fabry, 2015; Houze, 2014).

The backscattered signal received by the radar antenna is referred to as the radar reflectivity factor Z. It can also be obtained from the sixth moment of the number size distribution of the hydrometeors in the volume of air scanned by the radar. Assuming Rayleigh scattering and the simple case that all particles in the scanning volume are perfectly spherical liquid water droplets, the radar reflectivity factor is given by:

$$Z = 64 \int_0^\infty n_N(r_h) r_h^6 dr_h \approx 64 \sum_i n_N(r_{h,i}) r_{h,i}^6 \Delta r_{h,i} = 64 \sum_i N(r_{h,i}) r_{h,i}^6. \tag{10.8}$$

Here $n_N(r_h)$ is the hydrometeor number size distribution (Section 6.2.2) in $\mathrm{m^{-3}\,mm^{-1}}$, $r_{h,i}$ is given in mm, and $N(r_{h,i}) = n_N(r_{h,i})\Delta r_{h,i}$ is given in $\mathrm{m^{-3}}$. Let us assume a unit volume of air ($1\,\mathrm{m^3}$) with one raindrop with $r_h = 2.5$ mm. In this case, Z amounts to $64 N_{2.5\mathrm{mm}} r_{2.5\mathrm{mm}}^6 = 15\,625\,\mathrm{mm^6\,m^{-3}}$. Because the reflectivity is proportional to r_h^6 (sixth moment of the size distribution), the same Z value can be obtained from 15 625 uniform raindrops of 0.5 mm radius. Note that a 2.5 mm raindrop weighs only 0.065 g whereas the 15 625 raindrops of 0.5 mm radius weigh 8.18 g altogether. Thus, the return echo is dominated by the signal from the largest hydrometeors.

Certainly, the term r_h^6 in eq. (10.8) causes the values of Z to increase sharply with increasing r_h. Therefore, instead of displaying Z in $\mathrm{mm^6\,m^{-3}}$, it is more practical to display it on a logarithmic scale with base 10. The common unit for Z is

$$\mathrm{dBZ} = Z[\mathrm{dB}] = 10 \log_{10} \left(\frac{Z}{\mathrm{mm^6\,m^{-3}}} \right). \tag{10.9}$$

https://doi.org/10.1017/9781009485654.011 Published online by Cambridge University Press

Table 10.2 Typical values of Z for various hydrometeors, detected with either a cloud or a precipitation radar. Data based on Liu et al. (2008), Matrosov et al. (2009), Peters and Görsdorf (2010), Houze (2014) and Kopp et al. (2024).

Radar type	Object	Z values
Cloud radar	Cloud droplets	−40 to −20 dBZ
Cloud radar	Mixed-phase clouds	−20 to −10 dBZ
Cloud or precip. radar	Drizzle	−20 to 0 dBZ
Precipitation radar	Very light rain or light snow	0–10 dBZ
Precipitation radar	Moderate rain or heavier snow	10–30 dBZ
Precipitation radar	Melting snow or very heavy snow	30–45 dBZ
Precipitation radar	Moderate to heavy rain or graupel	30–60 dBZ
Precipitation radar	Hail	>55 dBZ

Typical values of Z for different hydrometeors are provided in Table 10.2. Because the power received by the radar antenna also depends on the phase of the hydrometeors, a better measure of the radar reflectivity is given by the equivalent reflectivity factor, which includes the complex index of reflection K:

$$Z_e = \frac{|K|^2}{0.93} Z. \tag{10.10}$$

From eq. (10.10) it follows that, for a given size, liquid hydrometeors have a factor 4.5 higher Z_e values than ice particles, that is, a reflectivity that is 6.5 dBZ higher in logarithmic units. This explains why in Table 10.2 values 0–10 dBZ refer to light snow but only very light rain and values 10–30 dBZ refer to heavier snow but only moderate rain.

Note that the radar reflectivity needs to be further corrected for the shape and density in case of frozen hydrometeors, rendering it highly variable in ice clouds (e.g., Maahn et al., 2015). In fact, the backscattering cross section $\sigma_B(r_h)$ of ice crystals is not only a function of their size, r_h, but also depends on the shape of the particles. While for small particles, the reflectivity is proportional to the sixth power of the particle size, using the soft sphere approach, the backscattering cross section of larger ice particles is only proportional to r_h^4 (Field et al., 2005). This is because the r_h^6 dependency of Rayleigh scattering in eq. (10.8) is partly compensated by a decrease in density with increasing ice hydrometeor size r_h, except for hailstones. Therefore, correction factors were developed that take the shape and density of the frozen hydrometeors into account (Löffler-Mang and Blahak, 2001).

Consider a snowfall event with 100 snowflakes per unit mass of air (m^{-3}) having equivalent radii 1.5 mm. According to eqs. (10.8) and (10.10), this would result in $Z_e = 42$ dBZ, which corresponds to melting snow or moderate to heavy rain (Table 10.2), even though there is no agreed international definition regarding rainfall intensity.

10.3.2 Relation of Radar Reflectivity to Precipitation Rate

Based on long-standing comparisons between radar reflectivities and rain gauge measurements, empirical relationships between radar reflectivity and rainfall rate are used at many

https://doi.org/10.1017/9781009485654.011 Published online by Cambridge University Press

Table 10.3 Radar reflectivity Z values as a function of rainfall rate R_r obtained using the empirical-approach Z_{MCH} (eq. 10.11) and the Marshall–Palmer distribution Z_{MP} (eq. 10.12).

R_r (mm h^{-1})	0.1	1	10	100
Z_{MCH} (mm^6 m^{-3})	9.5	300	9500	300 000
dBZ$_{MCH}$	10	25	40	55
dBZ$_{MP}$	10	25	39	54

weather services. For example, the Swiss weather service MeteoSwiss (MCH) uses the following relationship:

$$Z_{MCH} = c_{MCH} R_p^{1.5}, \tag{10.11}$$

with $c_{MCH} = 300\,\text{mm}^{4.5}\,\text{h}^{1.5}\,\text{m}^{-3}$ and R_p in mm h^{-1} denoting the rainfall rate in the case of liquid precipitation or the equivalent rainfall rate in the case of solid precipitation. As illustrated in the comparison between a single 2.5 mm raindrop and the many 0.5 mm raindrops earlier, neither this empirical relationship nor the exponential distributions for rain or snow (eqs. 10.1 and 10.3) hold for an individual precipitation event, but only when an average over many events is considered. Alternatively, Z can be related to R_p by assuming an average Marshall Palmer (MP) raindrop size distribution. Inserting eq. (10.1) into eq. (10.8) and using eq. (10.2) to replace Λ yields

$$Z_{MP} = 2^7 N_0 \frac{6!}{\Lambda^7} = N_0 \frac{6!}{(41)^7} R_p^{1.47} = c_{MP} R_p^{1.47}, \tag{10.12}$$

where $c_{MP} = 296\,\text{mm}^{4.53}\,\text{h}^{1.47}\,\text{m}^{-3}$. This equation is in very good agreement with the empirical formula used by MeteoSwiss. An example of the different values of Z obtained using the empirical relationship (eq. 10.11) or the Marshall–Palmer distribution (eq. 10.12) for various rainfall rates is given in Table 10.3.

10.3.3 Radar Images

Whereas earlier radars provided only a two-dimensional horizontal map as a function of time, nowadays more and more radars and subsequent data processing tools provide full three-dimensional information about cloud structures and precipitation patterns (Steiner et al., 1995; Starzec et al., 2017). Depending on how the radar antenna is pointed, different types of radar images are produced, including *plan position indicator* (PPI) radar images (Section 10.4.1) and *height-time indicator* (HTI) radar images (Section 10.4.1). PPI radar images refer to horizontal scans with the radar in the center pointing at a certain elevation angle (typically $< 3°$; Figure 10.4). The elevation angle to the horizontal plane is used to avoid obstacles, such as mountains and to avoid exposing humans to the emitted radiation. From PPI scans, a horizontal map of radar reflectivity is produced. The more hydrometeors that are encountered by the transmitted electromagnetic radiation from the radar, the more the radar signal becomes

https://doi.org/10.1017/9781009485654.011 Published online by Cambridge University Press

attenuated. Thus, a radar may not be able to detect multiple precipitating clouds if the transmitted radiation is attenuated by clouds closer to the radar antenna. Although the scattered signal per unit volume decreases with increasing penetration depth due to attenuation of the intensity of the emitted pulse, the reflectivity factor remains the same because it is a property of the precipitating cloud (eqs. 10.8 and 10.10). In addition, owing to the quadratic distance law, the intensity of the emitted pulse of electromagnetic radiation that is received per unit area decreases with increasing distance from the radar. An attenuated radar signal may cause problems, for example, in an area of vigorous convective storms or heavy rainfall, because the radar cannot detect what is behind them, and thus can bias radar-based rainfall estimates (Park et al., 2005). Because of the elevation angle of the PPI scan, the signals in the distance originate from higher altitudes, and precipitation from low clouds in the distance remains undetected. Typically, weather services operate a network of multiple radar systems with PPI scans to cover a wide area (Germann et al., 2022).

HTI, another type of radar image, is produced from vertically-pointing radars. HTI scans provide information on how the vertical distribution of hydrometeors changes with time, as shown in Figure 10.5. A HTI signal can be obtained from so-called Doppler radars (e.g., Görsdorf et al., 2015). Doppler radars offer the possibility of also determining the radial velocity of hydrometeors v_D along the beam path of the radar pulse from changes in the frequency of the returned signal induced by the backscattering object. Depending on the scan type, either the horizontal or vertical hydrometeor velocity can be obtained. For a vertically pointing radar, v_D is the net velocity, that is, the particle's fall velocity superimposed on the vertical wind speed (Figure 10.7). Thus, in order to estimate the fall velocities of the hydrometeors (Figure 9.18), the vertical wind speed needs to be known and subtracted (Orr and Kropfli, 1999).

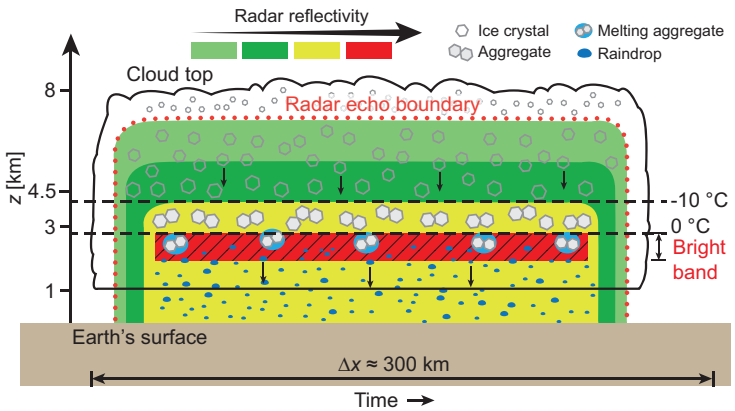


Figure 10.5 Schematic of the resulting HTI scan of a stratiform precipitation event passing a vertically pointing radar. The bold solid line marks the cloud boundary and the red dotted line marks the radar echo boundary. The region inside the radar echo boundary corresponds to different reflectivities as shown in the legend. The highest reflectivities are associated with the radar bright band (melting layer). Figure based on Chisholm and Renick (1972) and adapted from Houze (1981) with permission of Wiley.

https://doi.org/10.1017/9781009485654.011 Published online by Cambridge University Press

Range height indicator (RHI) is a combination of PPI and HTI by performing slanted scans at a constant azimuth angle, for instance, perpendicular to the main wind direction. They allow to obtain a full three-dimensional picture of precipitation events.

Note that the cloud boundary and the radar echo boundary do not coincide, as shown in Figure 10.5. This is because ice crystals in the upper levels of the cloud are too small to be detected by the precipitation radar. The same is true for the lateral edges of the precipitating cloud, where the hydrometeor sizes are smaller than in the cloud's interior due to entrainment and detrainment. While the cloud has a well-defined base at around 1 km altitude in Figure 10.5, the radar echo boundary extends down to the surface because precipitation reaches the surface.

10.4 Types of Precipitation

In terms of time scale, precipitation events can range from minutes, for convective showers, up to a few days, for stratiform precipitation originating from, for example, a low pressure system. These precipitation types also differ in their spatial scales.

To a first approximation, precipitation can be classified into continuous, large-scale (widespread), or *stratiform precipitation* and localized, small-scale (showery), or *convective precipitation*. Stratiform precipitation is associated with the large-scale ascent of air masses produced by frontal or orographic lifting or by large-scale horizontal convergence, mainly occurring at the meso-β scale (Figure 1.24) or larger. It is mainly produced in nimbostratus (Ns; Table 1.1) but also falls from dissipating cumulus congestus clouds that took on stratiform character, and from orographic clouds. Stratiform precipitation can last for several hours or days. In contrast, convective precipitation is associated with cumulus-scale convection in unstable air and is mostly produced in cumulonimbus (Cb) or cumulus congestus (Cu con, Table 1.1), mainly at the micro-α to the meso-γ scale. While the pattern of stratiform precipitation evolves relatively slowly, that of convective precipitation evolves rapidly and is short-lived.

An overview of the organization and microphysical structure of precipitating cloud systems is given by Houze and Hobbs (1982). The differences in spatial extent, intensity, and time scale of different precipitation types are mainly controlled by different vertical air motions and consequently cloud microphysical processes, which in turn are related to the various types of atmospheric instabilities (Chapter 4). Similarly, convective and stratiform precipitation differently affect the vertical profile of latent heating through transport of water (Houze Jr., 1989), affecting Earth's hydrological cycle, the atmospheric circulation, and ultimately climate.

One approach to distinguish stratiform precipitation from convective precipitation is by their vertical velocity w inside the cloud. Specifically, the distinction is usually made by comparing w with the terminal velocity of snowflakes ($v_{T,snow} \sim 1$ to $2\,\mathrm{m\,s^{-1}}$, Figure 9.18). In stratiform clouds, the vertical air motions are smaller than the characteristic terminal velocity of snow: $w < v_{T,snow}$ (Table 1.3) and therefore snowflakes can leave the cloud as precipitation. In contrast, in convective clouds, the vertical air motions are typically larger than the terminal velocity of snow: $w > v_{T,snow}$ (Houze, 2014) and therefore precipitation from convective clouds

https://doi.org/10.1017/9781009485654.011 Published online by Cambridge University Press

occurs in the form of rain, graupel, and hail. Distinguishing stratiform and convective clouds in this way was developed for midlatitudes, but it can also be applied to other regions. The criterion $w < 1$ to $2\,\mathrm{m\,s^{-1}}$ for stratiform precipitation also holds for warm clouds (clouds with no ice particles, Chapter 8), because cloud droplets have negligible fall velocities and raindrops have fall velocities considerably higher than $1–2\,\mathrm{m\,s^{-1}}$ (Figure 8.12).

While the updraft speed provides a relatively simple way to distinguish precipitation types, classifying precipitation as stratiform or convective can be challenging because the distinction between them is not always sharp. Certainly, widespread precipitation also shows small-scale structure. Specifically, spatial scales associated with the most intense precipitation peaks are often only a few kilometers in horizontal extent (e.g., Houze, 2014). Conversely, convective precipitation can extend over a large area if it originates from a multicell, a supercell, or a MCS. Therefore, convective precipitation can be more generally understood as having locally intense regions which range horizontally from 1 to 10 km and are separated from one another by areas with either no precipitation or only stratiform precipitation. Conversely, convectively generated Cb clouds or MCSs can also produce stratiform rain. This apparent contradiction can be understood from the evolution of the precipitation pattern during the lifecycle of convective clouds: While mature Cb clouds are associated with vigorous convective precipitation, the precipitation from older Cb clouds, where the vertical air motions are weaker, takes on stratiform character. Similarly, the fraction of stratiform precipitation in MCSs increases throughout their lifecycle (Houze, 1997), as will be discussed in Chapter 11.

The different updraft speeds in convective and stratiform precipitation systems lead to fundamentally different radar signatures between convective and stratiform precipitation. Thus, radar images can be used to distinguish the two different types of precipitation, as will be discussed in Sections 10.4.1 and 10.4.2.

10.4.1 Stratiform Precipitation

Plan Position Indicator Radar Image of Stratiform Precipitation

Figure 10.6 shows an example of a Doppler radar PPI image of the precipitation and horizontal wind speeds associated with the winter storm Lothar. Lothar hit northern France, southern Germany, Austria, Liechtenstein, and Switzerland on December 26, 1999 and caused considerable damage (Wernli et al., 2002). The radar image (Figure 10.6a) shows two rainbands with values >40 dBZ, indicating moderate to heavy rain or rimed particles (Table 10.2). As this precipitation was rather widespread horizontally, it can be characterized as stratiform. The horizontal velocities of the hydrometeors (Figure 10.6b) accompanying the precipitation event show wind speeds up to $50\,\mathrm{m\,s^{-1}}$ relative to the radar beam. The rainbands belong to a cold front that was embedded in a westerly flow. This can be inferred from the negative values west of the radar, indicating flow toward the radar, and positive values to the east of the radar, indicating flow away from it. The high radar reflectivity together with high wind speeds suggests the presence of convective rainbands, embedded in the stratiform precipitation, which could have been caused by slantwise displacement and symmetric instability (Section 4.7).

https://doi.org/10.1017/9781009485654.011 Published online by Cambridge University Press

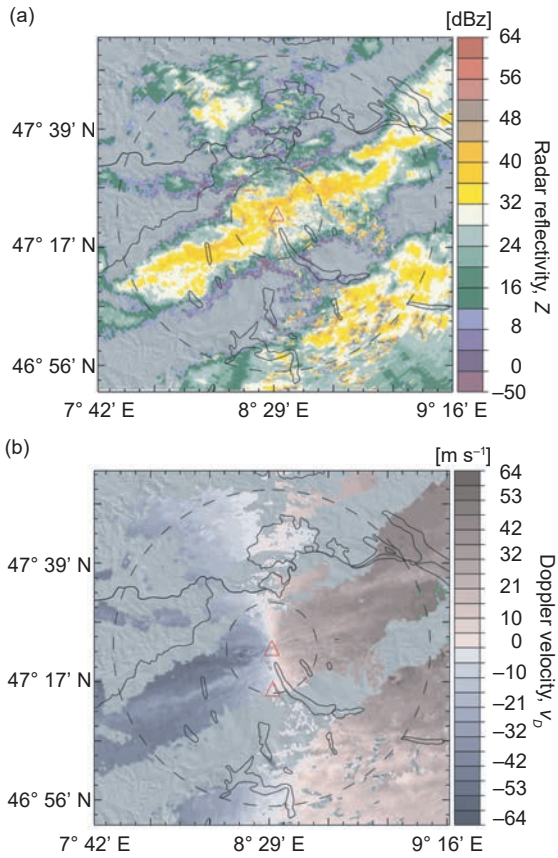


Figure 10.6 PPI images of (a) radar reflectivity and (b) Doppler velocity, scanned by the ETH radar in Zurich (triangle in the center) on December 26, 1999. The radar antenna was installed at 600 m above sea level and the scan was performed with a 1.5° elevation angle (Figure 10.4). The dashed circles mark PPI heights of 1 km (smaller circle) and 2 km above sea level (larger circle). In (b), the brown colors indicate velocities directed away from the radar and blue colors those directed toward the radar. Figure adapted from Wüest (2001).

Height-Time Indicator Radar Image of Stratiform Precipitation

While the radar image of stratiform precipitation appears homogeneously in the horizontal dimension, it often reveals a layered structure in the vertical dimension. In fact, stratiform precipitation from mixed-phase clouds, which can have temperatures above 0 °C at their bases, is characterized by a layer of high reflectivity, which gives rise to the so-called *radar bright band* in the signal of a vertically pointing radar. The bright band indicates the melting layer. A schematic illustration of the radar bright band associated with stratiform precipitation is shown in Figure 10.7 together with the microphysical processes during hydrometeor formation, growth, and settling (Houze, 2014).

Once ice crystals are formed, they grow by vapor deposition especially in the upper and colder part of the cloud where collisional growth processes are less efficient (Section 9.3). This is shown schematically in Figure 10.7 in the layer between points 1 and 2. Since this depositional growth is slow, Z_e increases only slightly with decreasing height. Indeed, in stratiform clouds, the time available for the growth of ice particles and sedimention from cloud top is about 1–3 h corresponding to the time it takes an ice particle that is falling at 1–2 m s^{-1} against the updraft to descend through a nimbostratus cloud with a vertical extent of 2–10 km (Table 1.3).

https://doi.org/10.1017/9781009485654.011 Published online by Cambridge University Press

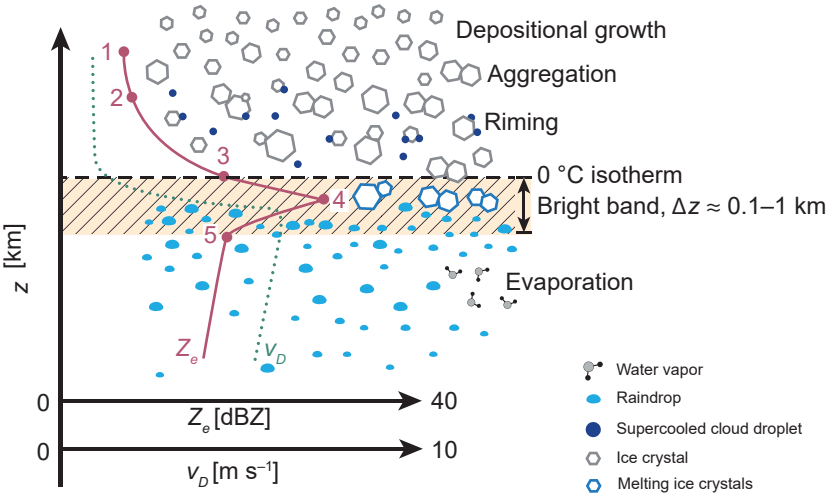


Figure 10.7 Schematic of a vertical profile of radar data for stratiform precipitation from a mixed-phase cloud. The solid red curve indicates the equivalent reflectivity factor Z_e (eq. 10.10) and the dotted green curve indicates the Doppler velocity v_D for a vertically pointing radar. The microphysical processes occurring in the layers between points 1 and 5 are explained in the text. Figure adapted from Houze (2014) with permission from Elsevier.

As soon as these ice crystals are large enough to start settling against the updraft in the cloud, growth processes involving collisions can also occur (Figure 10.5). Typically, when the falling ice particles descend slowly to a height within approximately 2.5 km of the 0 °C level, aggregation and riming are the dominant growth mechanisms, shown in Figure 10.7 between points 2 and 3. Aggregation increases in importance within ≈ 1 km (−10 to 0 °C) of the 0 °C level owing to the QLL (Section 9.5), that forms on the surface of the snowflakes. It causes the snowflakes to stick together by sintering and to form large irregularly shaped snowflakes. Growth by aggregation sharply increases Z_e because it is proportional to $\sim r_h^4$ for ice crystals (Field et al., 2005). Growth by riming also increases in the vicinity of the 0 °C level due to the more likely presence of supercooled cloud droplets (Figure 1.19).

In Figure 10.7, the layer between points 3 and 5 denotes the radar bright band, in which Z_e exceeds the values it has in the snow above it or in the rain below it by 10 dBZ_e. The increase in Z_e between points 3 and 4 is caused by melting, accounting for a 4.5 dBZ_e increase (eq. 10.10) along with continuing aggregation. In fact, Z_e is highest when snowflakes have acquired a liquid layer without having shrunk in size, as indicated by blue hexagons enclosing the aggregated ice particles. Thus, the radar bright band marks the layer in which the downward settling ice crystals are melting (Battan, 1973). The melting layer, and hence the radar bright band, have a vertical extent of 100 m to 1 km (Houze, 2014).

Below the bright band (point 4, Figure 10.7), continuous melting reduces the size of the snowflakes. The melting snowflakes become more compact and finally collapse or break apart, which reduces their sizes and Z_e. At the same time, the terminal velocity increases from 1 to 2 m s^{-1} for snowflakes to 5 to 10 m s^{-1} for raindrops (Figure 9.18). This corresponds to

https://doi.org/10.1017/9781009485654.011 Published online by Cambridge University Press

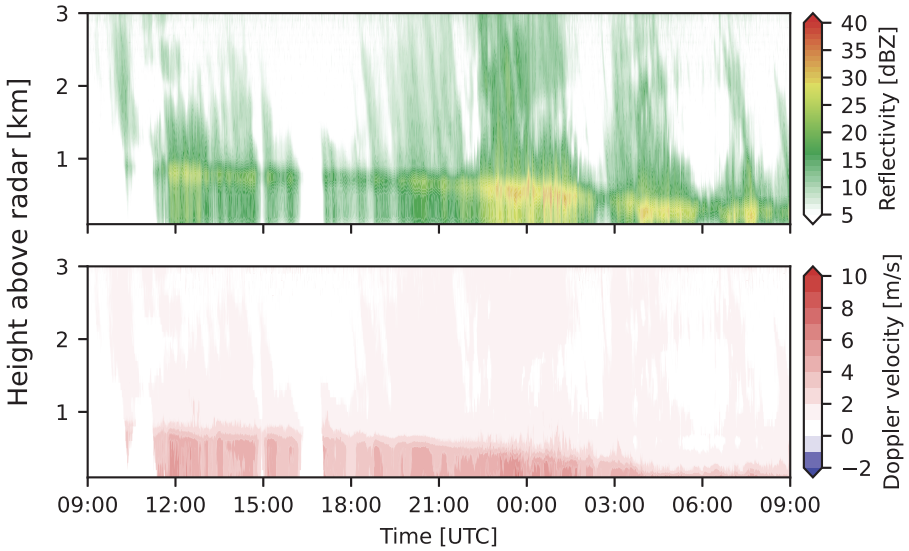


Figure 10.8 Example HTI scan, measured by a vertically pointing micro rain radar, of a stratiform precipitation event in Zurich, Switzerland, on January 5–6, 2024. Shown are (a) radar reflectivities and (b) Doppler velocities, where negative values indicate net upward motion. Measurements were taken by a micro rain radar operated at ETH Zürich. Data source: data.iac.ethz.ch/mrr/homepage/archive.html.

the sharp increase in the Doppler velocity v_D profile. The larger fall velocity of raindrops compared with snowflakes reduces their number concentration in space. Together with the ongoing melting and break-up of raindrops, this explains the reduction in radar reflectivity between points 4 and 5 in Figure 10.7. The layer below point 5 is characterized by rain. If the relative humidity below cloud drops to values below 100 % with respect to liquid water, the raindrops will start to evaporate, which further reduces v_D and Z_e.

An example of a radar bright band associated with a stratiform precipitation event in an HTI scan from a vertically pointing micro rain radar[5] is shown in Figure 10.8. In the reflectivity image of Figure 10.8a, the radar bright band is visible as a band of varying strength starting at approximately 900 m above ground and decreasing over time down to 200 m at the end of the shown event. Below the radar bright band, the positive Doppler velocities increase, indicating that the fall velocity of the hydrometeors switches from values $<2\,\mathrm{m\,s^{-1}}$, indicative for ice and snow (Figure 9.18), to values $>4\,\mathrm{m\,s^{-1}}$, indicative for rain (Figure 8.12).

Since the radar bright band is a typical indicator of stratiform precipitation, the entire event shown in Figure 10.8 could be classified as stratiform. More precisely, given the decreasing altitude of the melting layer (radar bright band) with time, this stratiform precipitation event was caused by the passage of a cold front over Central Europe. Even though this precipitation is event overall of stratiform character, there is still some intermittency with higher and lower reflectivities/fall speeds that indicate some embedded convection, for instance, between 22:30 UTC on January 5, 2024 and 1:30 UTC on January 6, 2024.

[5] https://iac.ethz.ch/the-institute/weather-stations.html

https://doi.org/10.1017/9781009485654.011 Published online by Cambridge University Press

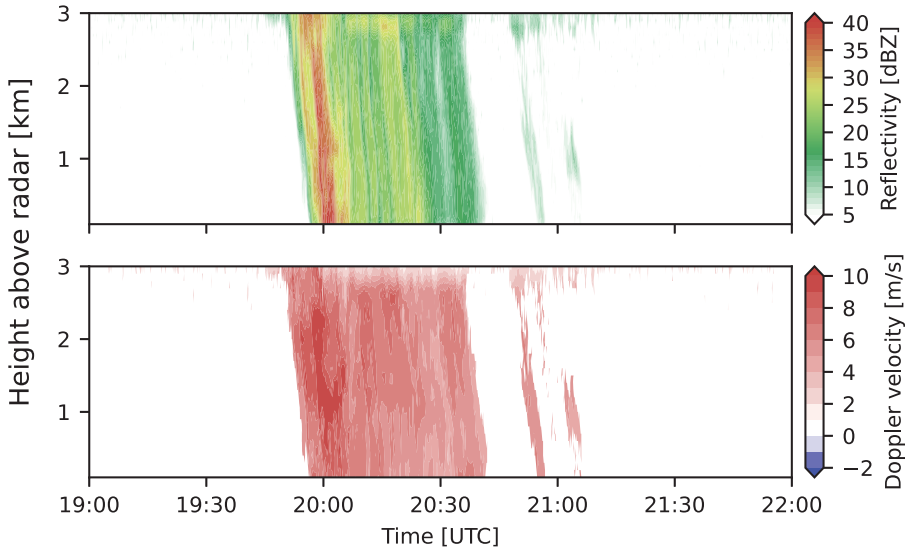


Figure 10.9 Height-time indicator radar image of convective cloud showers as observed in Zurich, Switzerland, on August 14, 2024: (a) radar reflectivity and (b) Doppler velocity, where negative values indicate net upward motion, as obtained from a micro rain radar operated at ETH Zürich. Data source: data.iac.ethz.ch/mrr/homepage/archive.html.

10.4.2 Convective Precipitation

Convective precipitation in summer is often a response to the Sun heating Earth's surface causing buoyancy in cases of weak synoptic flow, that is, when neither a high- nor low-pressure situation prevails. This is the case in Figure 10.9. Convective precipitation falls from Cu con and Cb clouds (Figure 1.2) or can result from embedded instabilities in stratiform clouds as described earlier. Isolated convective clouds occur over spatial scales of a few kilometers. Larger convective systems are complexes of this basic structure and will be discussed in Chapter 11. Inside Cu con and Cb, the updraft speeds are on the order of $10\,\mathrm{m\,s^{-1}}$ (Table 1.3 and Figure 10.9b) and thus exceed those of falling snow ($w > v_{T,snow}$). This keeps cloud droplets, ice crystals, snowflakes, and small raindrops floating or carried upward in the updraft. Only large raindrops and rimed structures (graupel and hail), for which the gravitational force is large enough, will fall against the updraft (Figure 9.18 and Table 9.2). Convective precipitation prevails in the tropics, during summer in midlatitudes, and over warm oceans. While the relative contribution of stratiform and convective precipitation to the total rain amount can vary depending on location and season (Rulfová and Kysel'y, 2013), the latter dominates over stratiform precipitation in the global annual mean (Schumacher and Houze, 2003; Tremblay, 2005).

The precipitation formation process is much more efficient in convective clouds than in stratiform clouds because of the higher updraft, and hence higher liquid water content in convective clouds (Table 1.3). In convective clouds, the collision–coalescence process is effective and dominates the hydrometeor growth in the lower levels of the cloud, where ice is absent. In shallow convection, in which the cloud top temperature is only slightly below 0 °C or warmer,

https://doi.org/10.1017/9781009485654.011 Published online by Cambridge University Press

such as typically found in the trade wind regions in the tropics, the collision–coalescence process can cause cloud droplets to grow rapidly until they are large enough to overcome the updraft speeds and to leave the cloud as raindrops (e.g., Aggarwal et al., 2016). In deeper convection, as well as in midlatitudes, ice-phase processes are normally involved in precipitation formation (e.g., Löhnert et al., 2015; Heymsfield et al., 2020). In these convective clouds, hydrometeors can also grow by riming, resulting in graupel and hail (Chapter 11). Because of the faster precipitation process in convective clouds, the typical time between the occurrence of a cumulus cloud and precipitation can be as short as 20–30 min (Saunders, 1965; Stephens and Haynes, 2007, Section 8.2).

Convective clouds have a radar echo distinctively different from stratiform clouds, as can be seen from a comparison of Figures 10.8 and 10.9. The radar echo of convective clouds evolves with time but is rather constant with altitude. In contrast, the radar echo of stratiform clouds changes with altitude but is rather constant in time.

Convective clouds are characterized by narrow updrafts that are typically a few kilometers or less in width. Convective showers can be as short as 10–15 min and occur in pulses, as shown in Figure 10.9. These well-defined vertical cores of intense reflectivity, so-called convective cells, a term coined by Byers and Braham (1948), consist of large hydrometeors (raindrops, graupel, and hailstones) and are typical of convective clouds. In the idealized vertical cross-section shown in Figure 10.10, a cell appears as a tall column of high reflectivity. Hence, the radar reflectivity does not change noticeably when crossing the 0 °C isotherm (thin solid line in Figure 10.10) but remains rather constant all the way to the surface. The reasons for the absence of a radar bright band in convective clouds are as follows: (i) the 0 °C isotherm is not a straight line but is shifted to higher levels in updrafts, due to the buoyant (warmer) air and to lower levels in downdrafts, owing to latent heat consumption by melting hydrometeors. (ii) convective clouds generally consist of rimed hydrometeors (graupel and hailstones), which have densities, and hence reflectivities, between those of pure water and snow (Table 1.2). (iii) hailstones produced by a convective storm can be much larger than all other precipitation-sized particles and hence dominate the radar reflectivity throughout the cloud (Table 10.2). Rimed hydrometeors do not melt as rapidly as snowflakes such that the melting layer is not visible in convective situations.

The white hydrometeors in Figure 10.10 show growing precipitation particles being carried upward by strong updrafts during the developing stage of a cumulus cloud until time t_4. Thereafter, the precipitation particles fall relative to the updraft and reach the ground at time t_6 when the cloud has reached the mature stage. In the dissipating stages of convective clouds (after t_6), the strong upward motion ceases and no longer carries precipitation particles upward or suspends them aloft. The fallout of the particles aloft due to the dying updrafts subsequently causes the core of maximum reflectivity to weaken. The precipitation then takes on a stratiform character, including a radar bright band as seen at t_7 in Figure 10.10 (Houze, 1997). At time t_n, only a dissipating cloud remains (the shape with the dashed outline).

In summary, the distinctively different radar structures of convective vs. stratiform precipitation allow meteorologists to classify radar echoes as either convective or stratiform (Houze, 1997).

https://doi.org/10.1017/9781009485654.011 Published online by Cambridge University Press

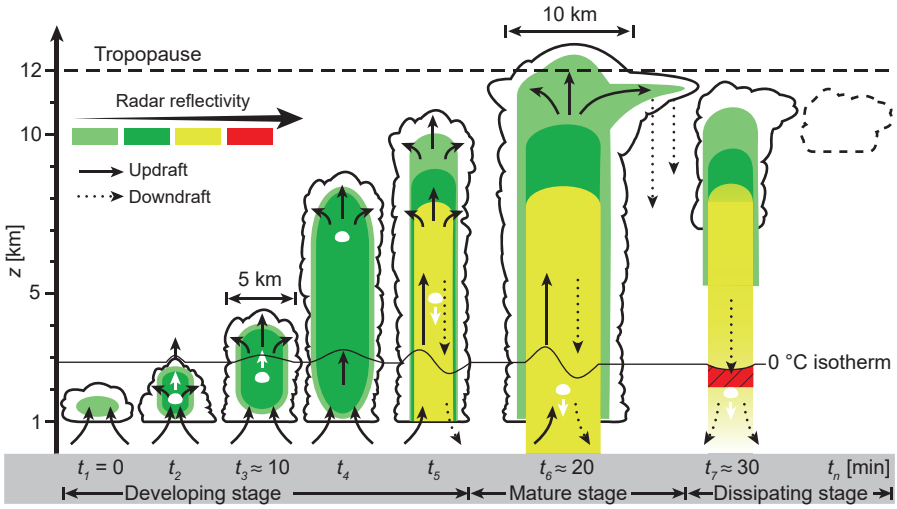


Figure 10.10 Schematic of the temporal evolution of a typical radar echo associated with a precipitating convective cloud. The bold solid outlines mark the cloud boundaries. The colored regions mark the radar echoes, whereby yellow and red colors refer to higher radar reflectivities. The solid and dotted arrows denote updraft and downdraft regions, respectively. The timeline in minutes gives a rough indication of the times associated with the single-cloud stages. The dashed outline at t_n indicates a dissipating cloud. The white disks denote the net direction of the hydrometeor movement. The stippling indicates the bright band. Figure adapted from Houze (1981) with permission of Wiley.

10.5 Synoptic and Mesoscale Structure of Precipitation

Even though low pressure systems are an example of synoptic-scale phenomena (Figure 1.24), they can exhibit mesoscale substructures. Prior to the development of radars, these mesoscale substructures were not necessarily resolved by the network of observational stations on which weather forecasts were traditionally based, because the weather station density is not high enough. An example of mesoscale substructures associated with synoptic-scale extratopical cyclones is rainbands (Houze et al., 1990). Rainbands denote the precipitation and cloud structure of a rainfall area that is large enough that an orientation can be assigned. Rainbands can be classified, among others, into wide cold frontal rainband (WCFR), narrow cold frontal rainband (NCFR) (Rutledge and Hobbs, 1984), and warm frontal rainband (WFR) (Houze et al., 1976), as shown in Figure 10.11. Rainbands in extratropical cyclones vary in spatial extent, having typical scales between 200 km and more than 800 km in length (Zhang and Schultz, 2023) and between 5 and 50 km in width (Houze and Hobbs, 1982).

The timings and locations of the precipitation areas relative to the surface fronts of an extratropical cyclone depend on the airflow, stability, moisture supply, and orographic influences. While climatologically banded precipitation makes up only 15% of all precipitation features over the United States, globally these features deliver 22% of the annual precipitation (Fairman et al., 2016).

https://doi.org/10.1017/9781009485654.011 Published online by Cambridge University Press

Rainbands themselves can be non-convective or only weakly convective[6] and can have embedded cells of heavy (convective) precipitation. Rainbands can also be associated with deep convective clouds, shallow convection in the planetary boundary layer, or they can originate at mid-levels in low-pressure systems.

In fact, heavy precipitation from convective clouds is often observed to be organized in lines or bands (Wang et al., 2014; de Orla-Barile et al., 2022). An example is depicted in Figure 10.11, where a WCFR and an embedded NCFR form underneath the Cb cloud due to lifting along the cold front. These rainbands cause most precipitation associated with frontal systems, and can vary in number, structure and intensity.

However, convective precipitation can also develop in unstable air without frontal lifting and can become organized in bands or lines unrelated to the synoptic pattern.

10.5.1 Norwegian Model of Extratropical Cyclones

Traditionally, precipitation associated with synoptic-scale extratropical cyclones was related to the clouds at the warm and cold fronts, with stratiform precipitation from Ns (Figure 1.4c) at the warm front and convective precipitation from Cb (Figure 1.4b) at the cold front, as schematically shown in Figure 10.11. This concept of the cyclogenesis, fronts, and associated cloud types is based on the so-called Norwegian cyclone model developed at the Bergen School of Meteorology (Bjerknes, 1919; Bjerknes and Solberg, 1922). The central idea of the Norwegian cyclone model is that a cyclone can be viewed as a perturbation on an existing frontal boundary. It was mainly developed for frontal structures near Earth's surface and hence does

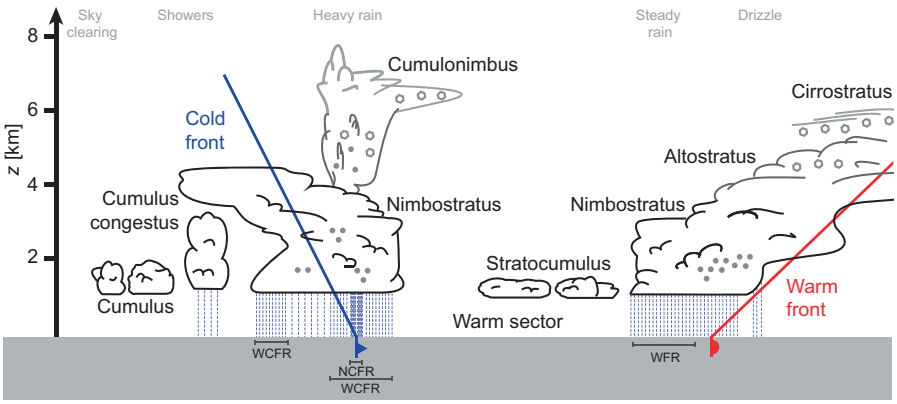


Figure 10.11 Schematic cross section of an extratropical cyclone (see line AB in the plan view of Figure 10.12b) with typical cloud types (Table 1.1) and rainbands. The red solid half disk denotes the surface warm front and the blue solid triangle the surface cold front. WCFR and NCFR denote the wide and narrow cold frontal rainbands and WFR the warm frontal rainband.

[6] https://glossary.ametsoc.org/wiki/Rainband

https://doi.org/10.1017/9781009485654.011 Published online by Cambridge University Press

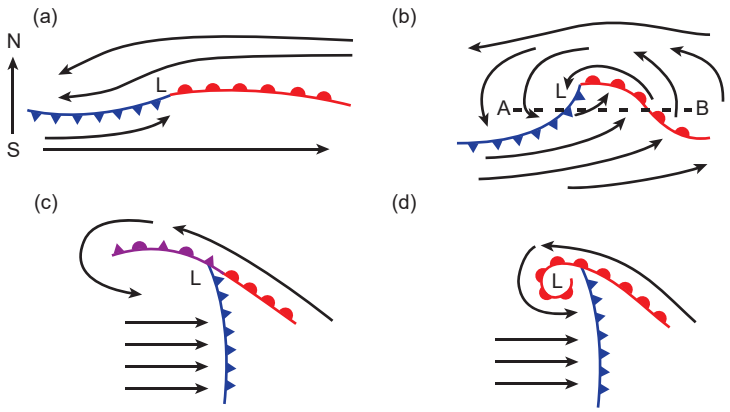


Figure 10.12 Schematic of the surface fronts and associated flow of the different cyclogenesis phases: (a) initial phase, (b) early phase, (c) the occluded phase, and (d) the T-bone frontal structure. The red half disks denote the surface warm fronts, the blue triangles the surface cold fronts, the purple symbols the occlusion, and the L marks the center of the low pressure system. A cross-section through the line AB is shown in Figure 10.11.

not capture their complete vertical structure. This model is based on synoptic weather patterns and on the concept that warm- and cold-air flows encounter each other at the polar front, where the warm subtropical air mass pushes polewards and the cold Arctic air mass pushes equatorwards, as schematically shown in Figure 10.12a. These motions cause the deformation of the polar front in the form of a wave. Ahead of the wave crest, the warm air pushes poleward and behind it, the cold air pushes equatorward (Figure 10.12b). If this wave disturbance develops further, it leads to a pressure drop in the center and causes well-developed warm and cold fronts. At the warm front, the warm air moves on top of the residing cold air. At the cold front, the cold air pushes itself underneath the warm air.

Whereas in the Norwegian cyclone model, all cyclones end in an occlusion, that is, the formation of an occluded front at the apex of the cyclonic wave, other studies suggest that the occlusion is still part of the evolution process of a developing cyclone (Schultz and Vaughan, 2011), as illustrated in Figure 10.12c. Some extratropical cyclones develop a so-called T-bone frontal structure, as shown in Figure 10.12d (Shapiro and Keyser, 1990). This structure is characterized by a warm front that is bent backwards and a cold front that moves perpendicular to the warm front. This T-bone frontal structure has also been identified in European cyclones of tropical origin (Dekker et al., 2018). However, still other extratropical cyclones show frontal structures that differ from the classical T-bone and occlusion structures, mainly because they develop only either a warm or a cold front, or because they have a strongly barotropic structure with very weak surface fronts or because they never develop a front during their lifetime (Schemm et al., 2018). This highlights the large variability of frontal structures in extratropical cyclones.

https://doi.org/10.1017/9781009485654.011 Published online by Cambridge University Press

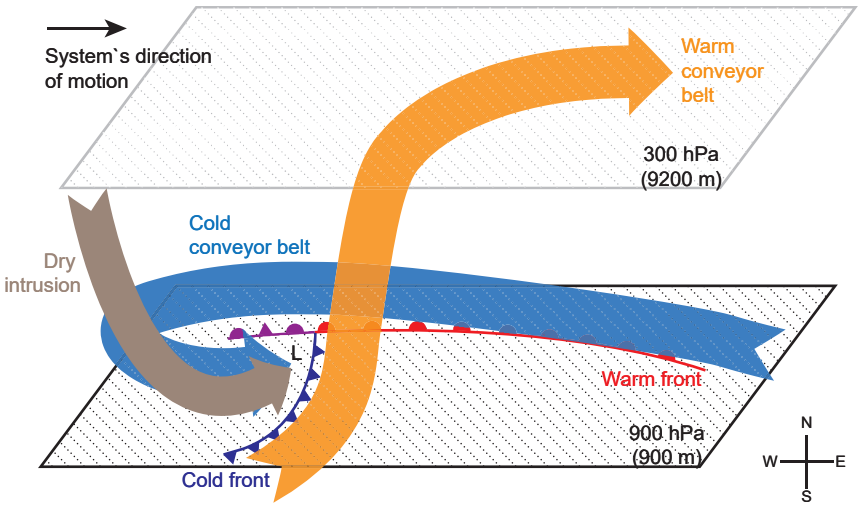


Figure 10.13 Schematic of an extratropical cyclone with a warm conveyor belt (WCB), shown as the orange arrow, cold conveyor belt (CCB), shown as the blue arrow, and a dry intrusion, shown as the brown arrow. The altitudes correspond to the average ascent of an air parcel in a WCB. Indicated heights are based on the WCB climatology by Madonna et al. (2014).

10.5.2 Conveyor Belt Approach

An alternative way to describe the (synoptic) pattern of extratropical cyclones and the associated frontal structures and precipitation patterns is provided by the concept of conveyor belts (e.g., Browning, 1985), shown schematically in Figure 10.13. Key features of the conveyor belt concept are the warm and cold conveyor belts (Carlson, 1980) that give rise to warm- and cold-frontal rainbands, as well as the dry intrusion, indicating the entrainment of dry air from the free troposphere into the low-pressure system.

The air movements along conveyor belts are relative to the movement of the low pressure system. As long as no condensation sets in, the potential temperature θ of the air is conserved and movement along the warm conveyor belt (WCB) takes place on isentropic surfaces (Figure 10.14a), which are sloped upward in Figure 10.14a. Once condensation commences, the latent heat release causes the warm air mass to rise on surfaces of constant equivalent potential temperature θ_e, causing the flow to become cross-isentropic, as illustrated in Figure 10.14b. At the frontal surface, the isentropic surfaces are closer together than elsewhere. As the air mass rises partly on isentropic θ surfaces and partly on equivalent isentropic θ_e surfaces, the frontal surface is sometimes defined in terms of θ surfaces and other times in terms of θ_e surfaces.

The WCB is highly relevant for total and extreme precipitation from extratropical cyclones (Pfahl et al., 2014). It originates typically within the boundary layer (~900 hPa) and experiences the largest ascent, of more than 600 hPa, within the cyclone. This ascent is caused by large-scale lifting ahead of or across the cold front. Air within the WCB originates partly from the southerly low-level jet ahead of the surface cold front. It flows along the length of the cold front, and ascends to higher levels.

https://doi.org/10.1017/9781009485654.011 Published online by Cambridge University Press

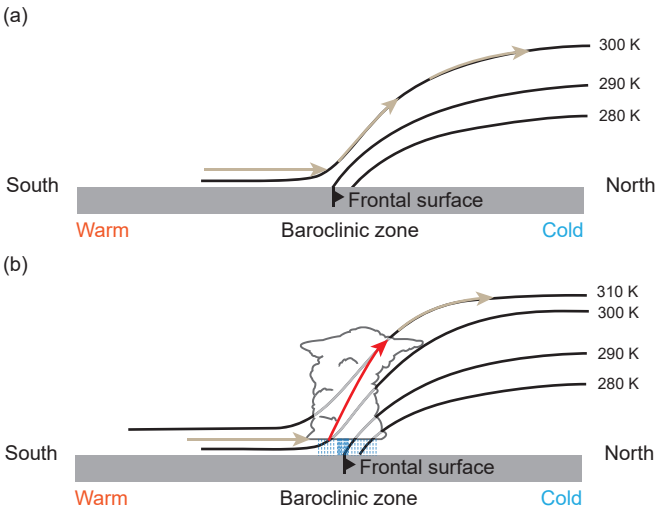


Figure 10.14 Schematic of a front in terms of θ-surfaces for (a) a dry ascending air parcel, and (b) an air parcel with latent heat release due to condensation, freezing, and deposition, causing the flow to become cross-isentropic.

In contrast to the WCB, the cold conveyor belt (CCB) is a coherent air stream in the lower troposphere, between 700 hPa and the surface, flowing on the cold side of the warm front, in a direction opposite to the movement of the cyclone. CCB trajectories frequently turn cyclonically around the center of the storm, as shown in Figure 10.13. A CCB is often associated with strong low-level winds and can trigger moisture transport along the bent-back part of the cold front, also referred to as the deformation zone, and can cause low-level wind jets (Schemm and Wernli, 2014).

Because the conveyor belt concept is used to describe the low pressure system as a synoptic-scale phenomenon, it cannot resolve the mesoscale structure of rainbands (Figure 10.11) and embedded convection (e.g., Oertel et al., 2020), resulting for instance, from symmetric instability (Figure 4.10).

10.5.3 Orographic Precipitation

Orographic precipitation is another example of a mesoscale phenomenon. It encompasses all precipitation events where topographic lifting comes into play (Gray and Seed, 2000; Houze Jr., 2012; Smith, 2019). Orographic precipitation can have a stratiform or convective character depending on the synoptic weather situation. If air is forced to rise over a mountain range in a stably stratified atmosphere and reaches its LCL (Section 3.4), then stratiform clouds may form on the upslope side (the windward side or luv), as shown in Figure 10.15a (Roe, 2005). When the air descends on the downslope side (lee), the clouds will evaporate again. Depending on the cloud thickness and the height of the mountain range, stratiform precipitation may fall on the windward side, the crest, or spill over to the lee side.

https://doi.org/10.1017/9781009485654.011 Published online by Cambridge University Press

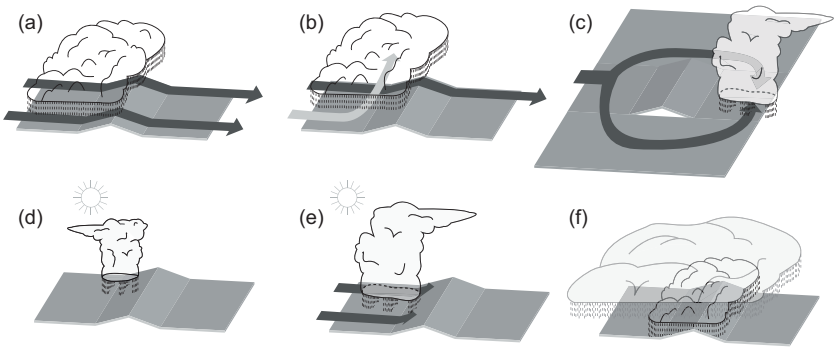


Figure 10.15 Schematic illustrations of different mechanisms of orographic precipitation. The dark gray arrows indicate the direction of the flow. (a) Stable upslope ascent, (b) partial blocking of an impinging air mass (light gray arrow), (c) lee-side convergence, (d) convection triggered by solar heating, (e) convection due to mechanical lifting above the level of free convection (LFC), and (f) seeder-feeder mechanism. Stippling below cloud denotes precipitation. Figure adapted and reprinted from Roe (2005) with permission of Annual Review of Earth and Planetary Sciences.

In Figure 10.15b, the flow is partially blocked, meaning that the atmosphere is either too stable or the flow is not strong enough for the lower-level flow to ascend over the mountain. It can either stagnate or get diverted around the mountain, the latter being indicated by the light gray arrow in Figure 10.15b. Convective clouds may be formed when the air diverges around the mountain and converges on the lee side, initiating rising motion (Figure 10.15c).

On sunny days, with weak synoptic flow, the sun warms the hillslope. This can lead to instabilities and trigger convection and cumulus clouds in various stages, as shown in Figure 10.15d. If the sun heats the sun-facing slopes and causes the air to rise, this air will be replaced by air from the valley. This mechanical lifting above the LFC can lead to cumulus clouds, as shown in Figure 10.15e. The up-valley wind is part of the mountain-valley wind system and reverses into a down-valley wind at night. This wind system is comparable to the land-sea breeze (Section 10.6), as both are caused by differential heating (mountain-valley versus land-ocean, respectively).

Another mechanism by which orography can cause (sometimes even heavy) precipitation is the so-called seeder-feeder mechanism (Dore et al., 1992; Purdy et al., 2005; Rössler et al., 2014). In the example shown in Figure 10.15f, the "seeder" cloud is at high levels and is undisturbed by the orography below. The cap cloud at low levels that is caused by orographic lifting by the mountain range would not have precipitated by itself because it is too shallow. However, it provides the "food" for the hydrometeors falling from the seeder cloud aloft and thus enhances precipitation from the seeder cloud (Gray and Seed, 2000; Proske et al., 2021; Ramelli et al., 2021).

In summary, depending on the instability associated with the formation of the orographic clouds and their liquid and ice water contents, stratiform and/or convective precipitation may fall from them.

https://doi.org/10.1017/9781009485654.011 Published online by Cambridge University Press

10.6 Precipitation in the Present and Future Climate

10.6.1 Clouds and Precipitation in Earth's Hydrological Cycle

Clouds and precipitation are important components of the hydrological cycle, as they transport water over large distances and supply water to the Earth surface (Peixóto and Oort, 1983; Trenberth et al., 2011; Douville et al., 2021). An illustration of the main components and fluxes of the hydrological cycle is shown in Figure 10.16. Water changes its phase from gaseous to liquid and/or solid and vice versa when moving through the hydrological cycle. While water resides for thousands of years in the oceans and in the continental ice shelves, its residence time in the atmosphere is about one week.

The lifetime of water molecules in the atmosphere denotes the time between evaporation and precipitation and is often referred to as atmospheric lifetime or residence time of water vapor. The average lifetime of water vapor in the troposphere is on the order of 9 days (Hartmann et al., 2016), but can vary considerably depending on the region (5–11 days), with shorter lifetimes in the extratropics (Peixóto and Oort, 1983; van der Ent and Tuinenburg, 2017). Next to geographical variation, it has also been shown that median, rather than mean, lifetimes, for example, 4 to 5 days in the extratropics (Sodemann, 2020), more consistently describe the residence time of water vapor in the atmosphere.

Atmospheric water vapor can be transported over large distances both horizontally and vertically. In fact, one third of the precipitation over land originates from evaporation over the oceans and not from local evaporation from the corresponding land masses. The water from excess precipitation over land then enters the oceans as run-off. The global annual mean

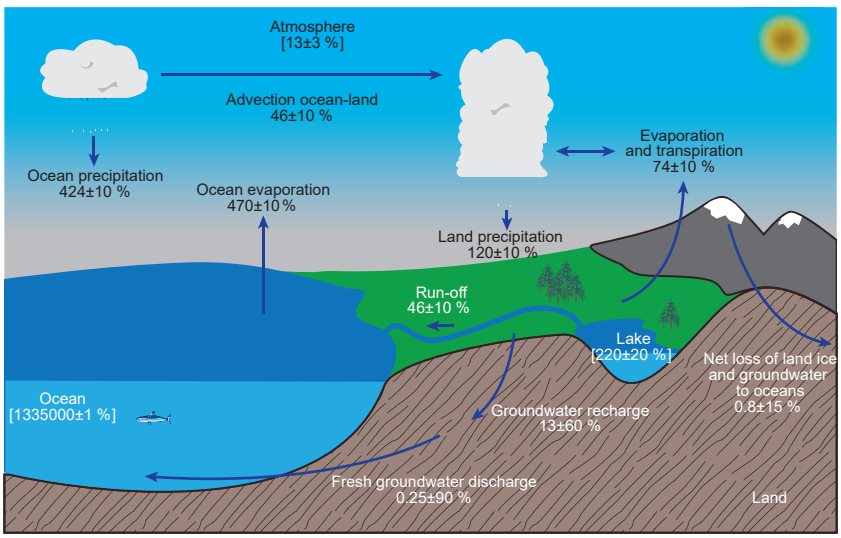


Figure 10.16 Schematic vertical cross section of various fluxes and reservoirs within the atmospheric branch of the hydrological cycle, with their annual average magnitudes according to the studies by Trenberth et al. (2011) and Douville et al. (2021). The water vapor reservoirs are given in 10^{15} and are denoted in brackets, while the fluxes in 10^{15} kg yr^{-1}.

https://doi.org/10.1017/9781009485654.011 Published online by Cambridge University Press

precipitation rate amounts to 2.91 mm day^{-1}, divided approximately into 2.27 mm day^{-1} over the oceans (71 %) and 0.64 mm day^{-1} over land (29 %) (Douville et al., 2021).

10.6.2 Distribution of Precipitation Type and Amount in the Current Climate

The geographical distribution of the total precipitation amount for DJF, JJA, and for the long-term annual mean from the Global Precipitation Climatology Project (GPCP) (Adler et al., 2003) is shown in Figure 10.17. The GPCP dataset combines data from rain gauge stations, satellites, and sounding observations to estimate monthly mean rainfall on a 2.5° × 2.5° global grid from 1979 to the present. The satellite data add necessary spatial detail over data-sparse regions over land and are crucial for estimating precipitation over the oceans.

Not surprisingly, the geographical distribution of precipitation bears some resemblance to the geographical distribution of total cloud cover discussed in Chapter 1. The largest amount of precipitation falls in the tropics, in the ITCZ and SPCZ, the same areas that are characterized by a large cloud cover (Figure 1.1). This precipitation is mostly of a convective nature, originating from isolated convective storms or larger precipitation complexes, such as MCSs, tropical depressions, tropical storms, and TCs (Chapter 11). By comparing the amount of precipitation in DJF with that in JJA, the seasonal cycle of the ITCZ becomes apparent. Its annually-averaged position is at around 5 °N, because convection is more vigorous over land than over oceans and the fraction of land masses is larger in the northern hemisphere than in the southern hemisphere. Because of the smaller heat capacity of land masses as compared with oceans, heating by the Sun warms the land masses more readily. During the day, this causes the air over land to become unstable and to rise. If the atmosphere is sufficiently moist, cumulus clouds will form. The more unstable and moist the atmosphere is, the deeper the cumulus clouds will be and the more they will precipitate (Chapter 5). The rising air over land is replaced by the adjacent air, often originating from the nearby oceans, which thereby provides a source of moisture. This effect can often be observed in midlatitudes during summer and is referred to as sea breeze (e.g., Huang et al., 2010). The circulation reverses to a land breeze during night time, when the land cools faster than the ocean.

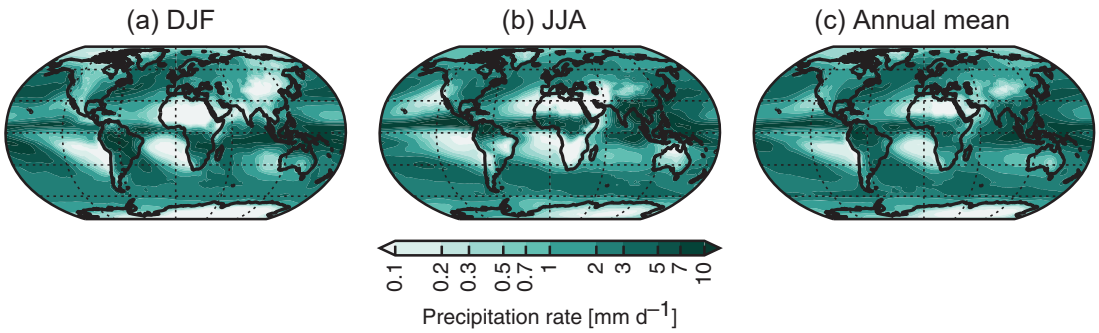


Figure 10.17 Seasonal mean precipitation rates as taken from Global Precipitation Climatology Project (GPCP) averaged over the period 1991–2020 for (a) December, January, February (DJF), (b) June, July, August (JJA), and (c) all months. Data source: https://psl.noaa.gov/data/gridded/data.gpcp.html.

https://doi.org/10.1017/9781009485654.011 Published online by Cambridge University Press

The same mechanism is responsible for the monsoon circulations on a larger scale and on a seasonal instead of a daily basis (Geen et al., 2020). Monsoon circulations exhibit the largest seasonal variations of all atmospheric circulation systems. The tropical Asian-Australian monsoon is the archetypal monsoon system. It encompasses the Indian or South Asian monsoon, the South China Sea monsoon, the Indochina Peninsula and Western North Pacific monsoon, the tropical Australian monsoon, and the Maritime Continent monsoon (Liu et al., 2004; Zhisheng et al., 2015). Subtropical monsoon systems include the East Asian monsoon, the African monsoon and the North American monsoon (Adams and Comrie, 1997). Heating of the Indian subcontinent and south-east Asia is so pronounced during JJA that a permanent low pressure system develops, causing the ITCZ to extend polewards up to 30 °N (Figure 10.17b). The Indian summer monsoon and the south-east Asian monsoon are associated with precipitation rates often in excess of 10 mm day^{-1} (Mitra et al., 2013). In DJF, when the ITCZ is south of the equator, deep convective clouds rise, and precipitate over the Indian ocean instead. During that period, a high-pressure system, which is associated with the northeast trade winds, develops over the Indian subcontinent . The high-pressure system is responsible for the negligible amounts of precipitation over the Indian subcontinent during DJF. The southward movement of the ITCZ is also seen in the location of precipitation over Africa, Central and South America in Figure 10.17b: Western Africa south of the Sahara and Central America receive most of their precipitation in JJA, whereas southern central Africa and Brazil receive most of their precipitation in DJF (Figure 10.17a).

Precipitation in the midlatitudes is mainly associated with frontal systems, especially with WCBs (Pfahl et al., 2014). Regions of high annual precipitation are found along the storm track regions (Figure 1.1). Convective showers and thunderstorms contribute to precipitation in midlatitudes, especially in their respective summer seasons over land (Figure 10.17). Steep orography causes orographic precipitation (Roe, 2005; Houze Jr., 2012), as evident at the coasts of Patagonia, the west coast of North America in DJF, and to a lesser degree also in Norway.

10.6.3 Trends in Past and Future Precipitation

Changes in annual precipitation amount are shown in Figure 10.18: Figure 10.18a shows changes over land for the period 1901–1984 obtained from the Global Precipitation Climatology Centre (GPCC). Figure 10.18b shows changes over land and ocean for 1985–2014 obtained from IPCC AR6 (Douville et al., 2021). The break of the time series in 1985 is because the cooling caused by aerosols, called global dimming (Section 12.1.1 and Wild (2016); Douville et al. (2021)), was largest in 1985. Since then, aerosol emissions in Europe and North America have declined, which has caused additional warming and, thus, enhanced trends in precipitation. In addition, the data coverage over the oceans was very sparse at the beginning and middle of the 20th century so precipitation trends before 1985 are shown only over land in the figure.

As precipitation can be very localized in space and time, trends in precipitation are not homogeneous. Nevertheless, one can see a trend toward increases in precipitation in midlatitudes and decreases in precipitation in the subtropics in Figure 10.18b. The decrease in

https://doi.org/10.1017/9781009485654.011 Published online by Cambridge University Press

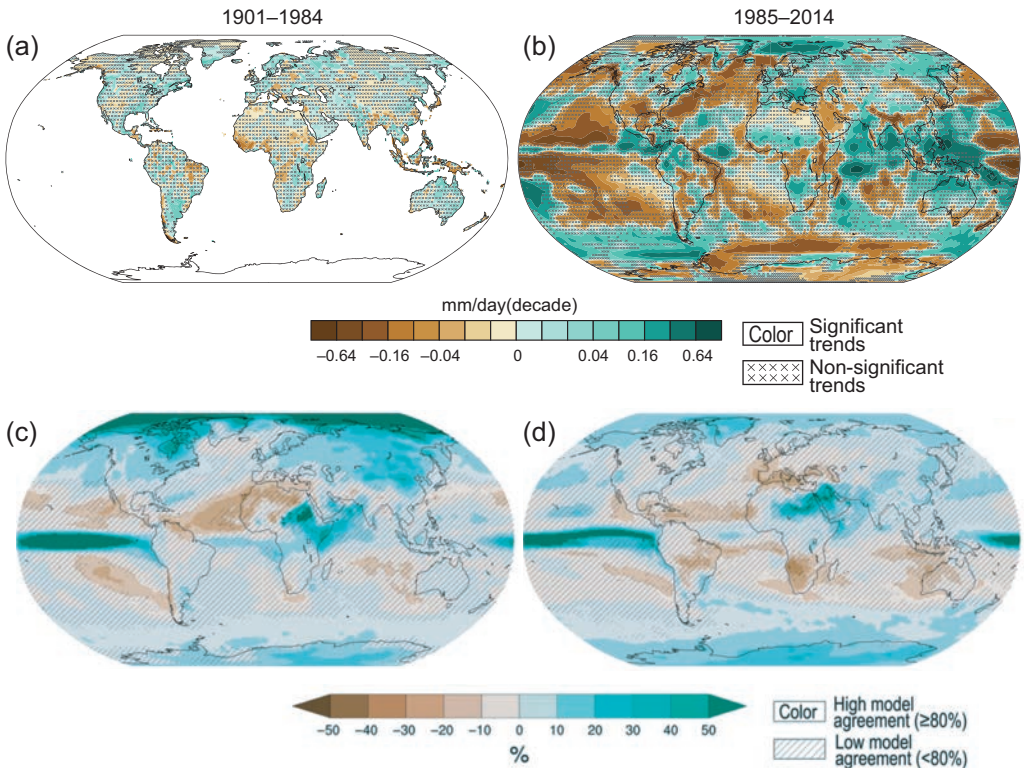


Figure 10.18 Trends in annual precipitation (a) over land from 1901 to 1984 and (b) over land and ocean from 1985 to 2014. Colour shades without gray crosses (stippling) correspond to the regions exceeding 10 % significance level. (c,d) show projected percentage changes of seasonal mean precipitation for the period 2081–2100 relative to the reference period 1995–2014 following the shared socio-economic pathway SSP2–4.5 forcing scenario for (c) DJF and (d) JJA. No hatching indicates regions with high model agreement, where ≥ 80 % of models agree on sign of precipitation change. (a,b): Figure 8.7 of Intergovermental Panel of Climate Change (IPCC) Assessment Report 6 (AR6) (Douville et al., 2021); (c,d): Figure 8.14 of IPCC AR6 (Douville et al., 2021).

precipitation is pronounced in regions that are already rather dry in the present climate, especially over the subtropics (Held and Soden, 2006; Chou et al., 2009). Over land, 11–41 % of the area shows a "dry gets drier, wet gets wetter" pattern while 10–35 % of the land area shows the opposite pattern (Greve et al., 2014; Xiong et al., 2022). The trends are more pronounced and significant since 1985, coinciding with the period during which the temperature increase has been largest (Masson-Delmotte et al., 2021).

In order to make projections about potential changes in precipitation patterns and magnitudes in the future, one needs to follow a particular *climate change scenario*. Climate change scenarios take several factors into account, such as demographic development, socio-economic development, and technological changes and innovations. Based on these factors, time series (pathways) of future emissions and/or concentrations of anthropogenic greenhouse gases and aerosol particles are projected. These projections are then used within climate models to simulate changes in climate, for example in temperature, precipitation, or cloud cover that

https://doi.org/10.1017/9781009485654.011 Published online by Cambridge University Press

result from the changes in these factors, referred to as anthropogenic forcing. As the future development of these factors is associated with large uncertainties, different scenarios of anthropogenic forcings must be interpreted as different possibilities of the resulting climate. In the IPCC AR6, scenarios are defined in terms of so-called *shared socio-economic pathways* (SSPs) (Meinshausen et al., 2020). Each SSP is characterized by an approximate level of *radiative forcing* (RF) in $\mathrm{W\,m^{-2}}$ in the year 2100 relative to the RF in 1750 (denoting pre-industrial conditions), on the basis of the scenario. The magnitude of the RF corresponding to an SSP is indicated by the number following the SSP. For instance, SSP2-4.5 corresponds to a positive RF of $4.5\,\mathrm{W\,m^{-2}}$ in the year 2100, defining a scenario with intermediate emissions of anthropogenic greenhouse gases. These SSPs are used in climate models of different complexity to project possible future climates and to estimate associated impacts for example on precipitation.

Estimated distribution of precipitation at the end of the 21st century obtained from such simulations when following the SSP2-4.5 scenario is shown in Figures 10.18c and d (Douville et al., 2021), for DJF and JJA, respectively. The data in Figures 10.18c and d are a multimodel mean over 38 coupled atmosphere-ocean global climate models (AOGCMs). These models are currently the most comprehensive in their representation of the climate.

The projections of precipitation changes differ between different AOGCMs. To account for this variability, regions with high model agreement (robust changes) are indicated without stippling in Figures 10.18c, d. Robust changes include increased precipitation in high latitudes and decreases in parts of the subtropics. This trends marks a continuation of the "dry gets drier, wet gets wetter" trend already seen in the 20th century (Figures 10.18a,b).

In DJF, northern Europe is expected to experience increases in precipitation, while the decrease in precipitation in southern Europe is not significant. In JJA, the opposite is true, with southern Europe expecting robust decreases in precipitation. In other words, the Mediterranean climate is expanding polewards in the SSP2-4.5 scenario.

Not only the global mean precipitation increases in a warmer climate, but also precipitation extremes are expected to intensify (IPCC, 2012; O'Gorman, 2015). Increases in precipitation extremes scale roughly with the Clausius–Clapeyron rate, that is, by 7 % per °C temperature increase (Li et al., 2021). In the case of convective precipitation, the rate might even exceed this value (Berg et al., 2013).

In summary, future changes in precipitation have a distinct geographic pattern: there will be regions in which precipitation increases, does not change at all or even decreases. However, the contrast between dry and wet regions and dry and wet seasons is likely to increase in most parts of the world in a warmer climate (Collins et al., 2013).

10.6.4 Extreme Precipitation

Heavy rain, high winds, and snow storms are examples of mesoscale weather and of extreme events. Radars still face challenges measuring small-scale rainfall extremes as they tend to underestimate rainfall as compared to rain gauges (Schleiss et al., 2020). Larger-scale flooding is preceded by continuous precipitation over hours to days. For instance, the extreme flood in Western Europe in July 2021 was part of a cut-off extratropical low pressure system and

https://doi.org/10.1017/9781009485654.011 Published online by Cambridge University Press

progressed down the rivers Ahr and Erft in Germany and the Meuse in Belgium. It caused several days of heavy rain (e.g., Tradowsky et al., 2023). Another example is the Cévennes episode that caused severe flooding in Southern France and Italy in October 2024. It was also triggered by a cut-off low pressure system that channelled warm and moist air from the Mediterranean Sea to France and Italy. Record precipitation rates were more than 500 mm in 24 h in Southern France[7]. A few weeks later, the warm and moist air from the Mediterranean Sea caused flash floods in Valencia, Spain, again with precipitation rates close to 500 mm, but this time in only 8 h[8].

For extreme events, even a single, strong convective storm lasting for 1 h might be sufficient to cause flash floods. Regions that are particularly susceptible to flash floods are small and steep catchments, as present in the southern Alps, in the Rocky Mountains (e.g., Friedrich et al., 2016), or in California (de Orla-Barile et al., 2022). A devastating example for high-intensity precipitation from a NCFR occurred in Southern California in January 2018, the Montecito debris flow (Oakley et al., 2018). More details on the formation of convective storms will be provided in Chapter 11.

10.7 Artificial Weather Modification

Extremes, such as precipitation in the form of hail as well as the absence of precipitation, can cause problems for society. As an example, hail damage is a large risk for agriculture because hail exceeding 2 cm in diameter can seriously damage crops and destroy entire harvests (Section 11.4), with important implications for agriculture and the food supply system. On the contrary, some areas suffer from too little precipitation. In both cases, deliberate weather modification is being exploited, the basics of which we will outline here.

The most efficient way to turn a non-precipitating cloud into a precipitating one is by introducing INPs into a supercooled liquid water cloud, initiating the Wegener–Bergeron–Findeisen process (Section 3.5.3). The idea behind such glaciogenic cloud seeding was provided by the early laboratory experiments showing that silver iodide (AgI) can nucleate ice effectively (Vonnegut, 1947; Marcolli et al., 2016, Section 9.1.6).

An atmospheric example of the Wegener–Bergeron–Findeisen is a so-called *hole-punch cloud* (Figure 10.19). Hole-punch clouds can form when ascending airplanes fly through a thin supercooled altostratus layer, because the turbulence above the airplane wings and behind the aircraft can cause temperature decreases of more than 10 °C, which can be sufficient to initiate ice nucleation (Heymsfield et al., 2010, 2011).

Invoking the Wegener–Bergeron–Findeisen proccess to trigger precipitation formation and to increase the snow pack in the Rocky Mountains in the Western USA has been exploited by French et al. (2018); Friedrich et al. (2020). It is referred to as *wintertime orographic cloud seeding* (Rauber et al., 2019). The same concept was used to understand the initiation and

[7] www.meteosuisse.admin.ch/portrait/meteosuisse-blog/fr/2024/10/episode-cevenol-octobre-2024-foehn.html
[8] https://earthobservatory.nasa.gov/images/153533/valencia-floods

https://doi.org/10.1017/9781009485654.011 Published online by Cambridge University Press



Figure 10.19 Photograph of a hole-punch cloud, taken by Fabian Mahrt.

growth of ice crystals in supercooled low stratus clouds over the Swiss Plateau (Henneberger et al., 2023; Ramelli et al., 2024).

At $T > 0\,°C$, hygroscopic cloud seeding is used to enhance precipitation formation by accelerating droplet growth due to collision–coalescence. This is typically accomplished by injecting hygroscopic aerosol particles at cloud base that are larger than the background aerosol (giant CCN). Due to the uncertainties in the efficiency of the collision–coalescence process, the efficiency of hygroscopic seeding depends on the size, chemical composition, and number concentration of the seeding particles and the initial state of the cloud.

Although laboratory experiments, field observations, and simulations have demonstrated the potential for glaciogenic and hygroscopic cloud seeding to modify cloud properties, the efficiency of these techniques and the impacts on cloud–precipitation–radiation interactions remain uncertain (Chen et al., 2022). Ideas to reduce hail damage will be discussed in Section 11.4.2.

https://doi.org/10.1017/9781009485654.011 Published online by Cambridge University Press